2021 MERIT Self-directed joint research

Direct Observation of Ultra-High Resolution Magnetic fields in Centrosymmetric Ultrasmall-Skyrmion-Hosting Novel Material

Satoko Toyama[1], Haruto Yoshimochi[2]
[1] Shibata laboratory, Department of Material engineering
[2] Seki laboratory, Department of Applied physics

Authors Introduction

Satoko Toyama：Specializes in electromagnetic fields imaging by scanning transmission electron microscopy (STEM). She carried out the atomic structure and magnetic fields observation of $GdRu_2Ge_2$ using STEM.

Haruto Yoshimochi：Specializes in synthesizing and analyzing magnetic skyrmion-hosting materials using magnetic transport measurements. In this joint research, he carried out the single crystal synthesis and X-ray diffraction measurement of $GdRu_2Ge_2$.

Abstract

Magnetic skyrmions, which are topologically protected spin swirling structures, have attracted much attention as candidates for next-generation magnetic memory applications. Recently, a novel mechanism for the skyrmion formation has been proposed that overturns the conventional theory based on the Dzyaloshinskii-Moriya interaction. In particular, the multi-step topological magnetic phase transitions were discovered in centrosymmetric tetragonal itinerant magnet $GdRu_2Ge_2$ based on such a novel mechanism. In this study, we attempted to directly reveal the transition process of the series of magnetic phases in $GdRu_2Ge_2$ using the imaging technique of local magnetic fields with scanning transmission electron microscopy.

Introduction

Magnetic skyrmions, topologically protected spin swirling structures, have attracted attention for next-generation magnetic memory applications[1–4]. Previously, extensive studies have successfully identified skyrmion-hosting materials with non-centrosymmetric systems[5–9]. These asymmetries cause the relativistic Dzyaloshinskii-Moriya (DM) interaction, which inherently prefers twisted spin configurations and plays a crucial role in the formation of magnetic skyrmions. However, the recent theoretical studies suggest that the novel skyrmions can be formed with the completely different mechanisms from the conventional one. In particular, nanometric skyrmions with diameters one order of magnitude smaller than conventional ones can be realized by means of the itinerant-electron-mediated spin interactions on the highly symmetric lattice system[10–12]. Recent intensive exploration of Gd alloy systems has led to the discovery of such a new-type skyrmions[13,14]. Moreover, in 2020, the smallest skyrmion ever with a diameter of 1.9 nm was reported in a centrosymmetric tetragonal magnet $GdRu_2Si_2$ with a new-type formation mechanism[15,16].

The research group of author 2 discovered the multiple topological magnetic phases in $GdRu_2Ge_2$, which is related compound to $GdRu_2Si_2$, using the resonant X-ray scattering experiment[17]. In addition, the successive process of topological magnetic phase transition can be explained by the multi-step transition of meron/antimeron structures, the topological structures characterized by half-integer topological numbers.

At this stage, the above magnetic structures were determined based on the measurements in reciprocal information using the resonant X-ray scattering experiment. However, the local magnetic structures such as domain walls, which are not measurable with X-ray scattering, are also very important for the comprehensive understanding of the versatile magnetic phase transitions in $GdRu_2Ge_2$. Therefore, characterization techniques that can visualize local magnetic fields at a high spatial resolution are in high demand.

Recently, real-space magnetic field imaging using scanning transmission electron microscopy (STEM) has been rapidly developed[18]. STEM is a technique for acquiring information about a sample by scanning a finely focused electron probe over the sample and measuring the transmitted electrons at each point. Differential phase contrast (DPC) STEM is one of the STEM techniques that measures the momentum transfer of transmitted electrons and visualizes local electromagnetic fields inside the specimen. It has been demonstrated that DPC STEM can visualize electromagnetic fields of various materials and devices, such as electric fields inside electronic devices[19,20], electric fields of atomic nucleus[21,22], the atomic magnetic structure of antiferromagnetic materials[23], and magnetic skyrmions[24]. Those studies suggested that DPC STEM has the potential to elucidate the complicated magnetic structures of $GdRu_2Ge_2$ in real-space. However, magnetic field observation for obtaining various phases of $GdRu_2Ge_2$ requires the strict condition of under 1 nm resolution, Helium temperature, and applying 0-2T magnetic field. Since these conditions are extremely challenging, there have been no successful experiments acquiring various phases of such samples. One of the striking points is to achieve both a high-resolution and zero external magnetic fields. In ordinary high-resolution electron microscopes, a strong magnetic field of a few T is forcibly applied by a magnetic lens for acquiring a fine convergent electron beam. Therefore, observation of magnetic fields has been realized only for like skyrmions with a size of about 100 nm due to DM interaction[2] or under high external magnetic field conditions[15]. The author 1's group has developed the world's first electron microscope that enables sub-angstrom resolution observation in a magnetic field-free environment[25]. In addition, author 1 is developing a high-resolution electromagnetic field imaging method. It is expected that the above changing conditions can be achieved using these methods.

In this study, we performed high-resolution observation of the magnetic structure of $GdRu_2Ge_2$ by scanning transmission electron microscopy to clarify the various local structural changes associated with the various topological phase transitions.

Experimental Procedure/Result

■ Synthesis of single crystal・Crystal evaluation

Polycrystalline samples of $GdRu_2Ge_2$ were prepared by the arc-melting technique from stoichiometric amount of pure Gd, Ru, and Ge pieces using a water-cooled copper crucible under an Ar atmosphere. Bulk single crystals were grown in a floating zone furnace under Ar gas flow[26].

The purity of the samples was confirmed by the powder X-ray diffraction, and the crystal orientation was determined using the Laue X-ray method. The obtained diffraction pattern by the powder X-ray

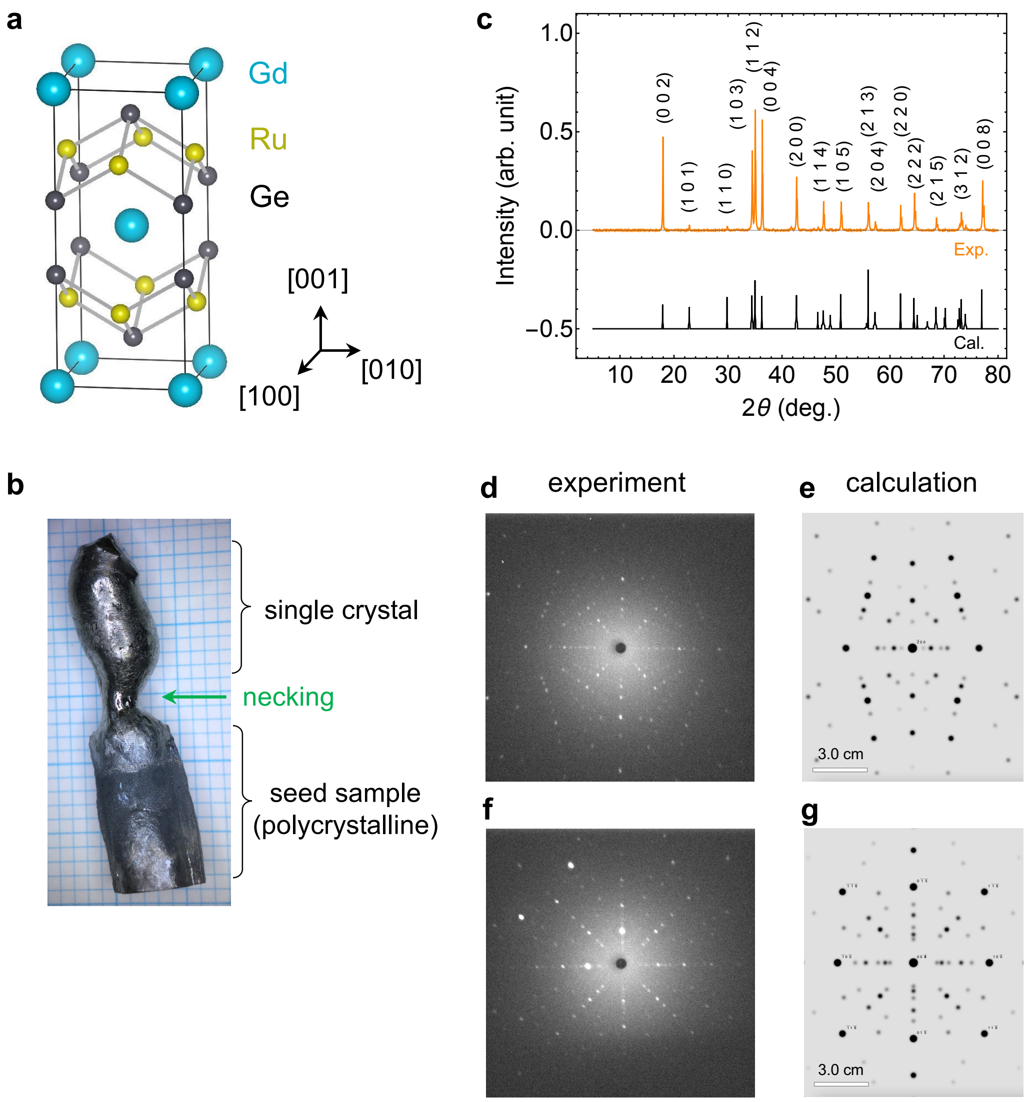

Fig. 1: **a**, Crystal structure of $GdRu_2Ge_2$ drawn by VESTA. **b**, Single crystal of $GdRu_2Ge_2$ synthesized by Floating-Zone method. The below is seed crystal and the upper is synthesized single crystal. Green arrow indicates the necking part for the purpose of aligning the domain of the single crystal. **c**, Powder X-ray diffraction pattern of the polycrystalline. **d-g**, Experimentally obtained Laue X-ray diffraction patterns (**d**,**f**) and corresponding ones obtained by theoretical calculation (**e**,**g**). **d**,**e** (**f**,**g**) are the patterns of *a*-plane (*c*-plane).

diffraction is shown in Fig. 1**c**. Experimentally obtained pattern is in very good agreement with the theoretical one, which guarantees the cleanness of the single crystal. Next, we show the Laue X-ray diffraction patterns in Fig. 1**d-g**. They agree well with the theoretically calculated diffraction patterns, which suggests the high-quality crystals with aligned domain.

■ Magnetization measurement

To confirm the magnetic property of the obtained single crystals, we performed magnetization measurement with Magnetic Property Measurement System (MPMS, Quantum Design).

Overall magnetization profiles are shown in Fig. 2**a-d**. The temperature dependence of the magnetic susceptibility under $B \parallel [001]$ shows $T_{\mathrm{N}} = 32.8$ K and $\Theta_{\mathrm{CW}} = 39.4$ K, which is almost consistent with the previous report ($T_{\mathrm{N}} = 33$ K、 $\Theta_{\mathrm{CW}} = 40$ K) [26]. Next, the magnetic field dependence of the magnetization is shown in Fig. 2**b**, which shows the magnetic property with easy-axis magnetic anisotropy. As shown in Fig. 2**c**, the magnetic field dependence under $B \parallel [001]$ shows step-like

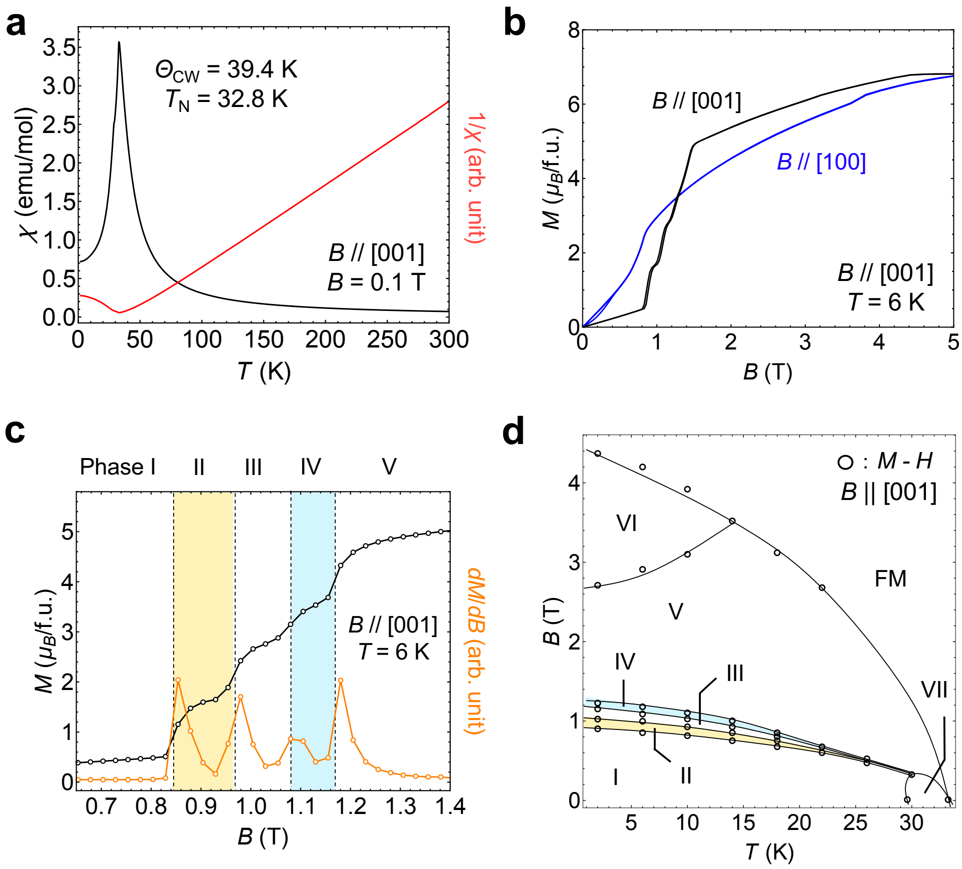

Fig. 2: **a**, Temperature dependence of magnetic susceptibility of $GdRu_2Ge_2$ under $B \parallel [001]$, $B = 0.1$ T. **b**, Magnetic field dependence of magnetization under $B \parallel [100]$ and $B \parallel [001]$ under $T = 6$ K. **c**, Magnetic field dependence of magnetization under $B \parallel [001]$, $T = 6$ K. Phases II and IV are highlighted with the colored shadow. **d**, Magnetic phase diagram determined by the magnetization measurement under $B \parallel [001]$.

anomalies, indicating the existence of multiple topological magnetic phases. The overall magnetic phase diagram is summarized in Fig. 2**d**, in good agreement with the previous report[17]. It is considered that the topological magnetic phase is realized in phases II IV, highlighted with the colored shadow of blue and yellow. From the above results of sample evaluation and magnetization measurement, it is concluded that $GdRu_2Ge_2$ single crystal with good quality was successfully obtained.

- HAADF STEM observation

High angle annular dark field (HAADF) STEM is an imaging technique that selectively detects transmitted electrons that are inelastically scattered at a high-angle using a ring-shaped detector[27,28]. Figure 3 shows a schematic representation of HAADF STEM. HAADF STEM imaging provides a contrast proportional to about the square of the atomic number. Since the image is robust to experimental conditions such as aberration, defocus, misalignment, and sample thickness, HAADF STEM is now popular for structural observation.

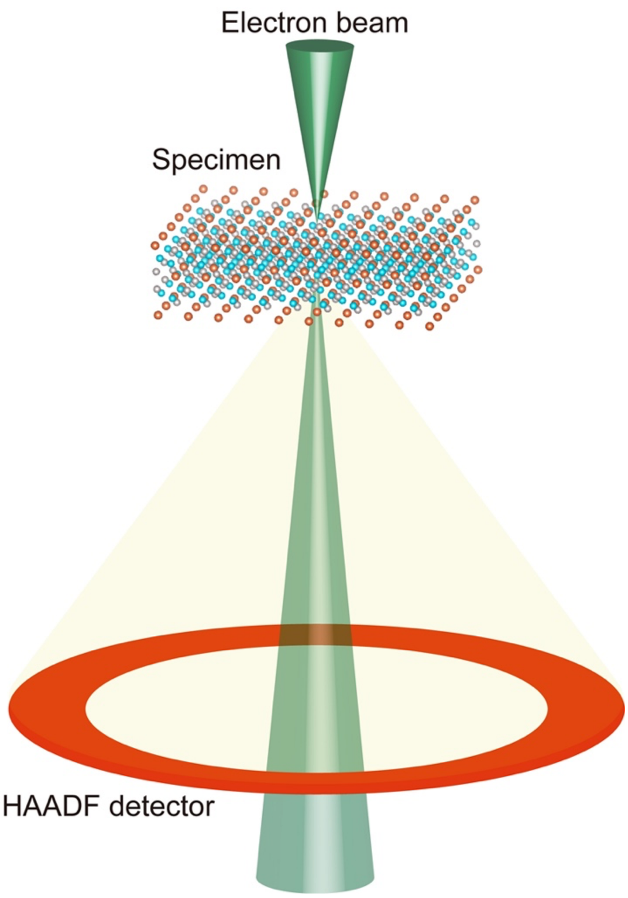

Fig. 3: Schematic of HAADF STEM. The configuration of HAADF detector respect to the sample is schematically shown.

Atomic-resolution HAADF STEM observation was performed for the confirmation of local structures of a $GdRu_2Ge_2$ sample in real-space. The sample was thinned on the *c*-plane using mechanical and Ar ion polishing. The newly developed STEM (JEOL Ltd.) equipped with magnetic field-free lenses[25] was used. The accelerating voltage and convergent-semi angle are set to 200 kV and 20 mrad, respectively. Figures 4 **a** and **b** show the HAADF images of the $GdRu_2Ge_2$ sample. As mentioned above, HAADF STEM provides a contrast corresponding to the atomic number, so the bright points are considered to be Gd (Ge) atomic columns and the relatively dark points are considered to be Ru atomic columns. The model of the crystal structure is also shown in Fig. 4**b**. These results confirm that the local structure of the observed sample is consistent with the structure obtained with X-ray diffraction.

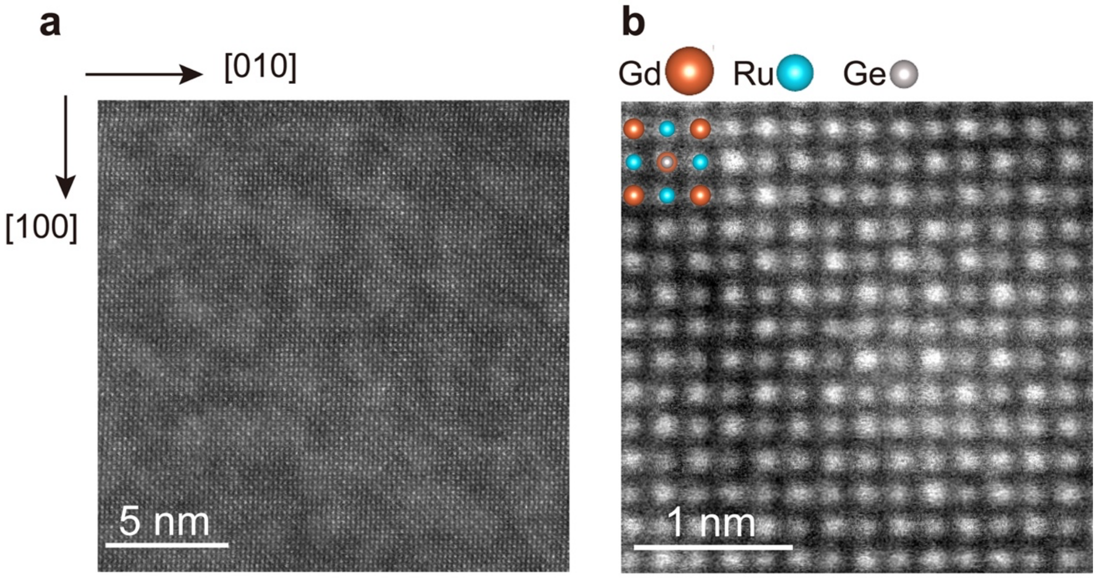

Fig. 4: **a**, Low mag and **b**, high mag HAADF STEM images of the $GdRu_2Ge_2$ sample. The model of the crystal structure is also shown in **b**.

■ DPC STEM observation

Figure 5 shows a schematic representation of DPC STEM. DPC STEM is an imaging technique to detect differential phase (momentum transfer) of the transmitted electrons. The imaging principles of DPC STEM are shown below. When an incident electron transmits through a sample, only the phase can be assumed to change, ignoring thermal diffuse scattering and dynamical diffraction effects (phase-object approximation). In such a case, the deflection of transmitted electrons can be regarded as a momentum transfer due to the internal magnetic field of the sample. Considering the electron as a classical particle, the momentum transfer of the transmitted electron is the sample magnetic fields integrated with the incident direction multiplied by a constant. Based on Ehrenfest's theorem[29], which states that even quantum systems can be described classically in terms of their expectation values, the relationship described above holds for quantum systems if the momentum transfer and the magnetic field are replaced with their expectation values. In that case, the deflection angle of transmitted electrons is synonymous with measuring the center of mass of the transmitted electron disk[30,31]. The measurement of the center of mass can be performed with specific detectors, which are called segmented detectors. A segmented detector should be introduced below the sample and can measure the electron intensity illuminated on each segment. Figure 5**b** shows a schematic of a 40-segmented detector and deflected transmitted electron disk. The center of mass of the transmitted electron disk can be measured by adding the electron intensities weighed by the geometric center of mass of each segment. Real-space mapping of the magnetic fields inside a sample is obtained by such measurements at each point on the sample.

The magnetic field observation of $GdRu_2Ge_2$ was performed using the same sample and STEM as in the previous section. The accelerating voltage and convergent-semi angle were set as 200 kV and 1 mrad, respectively. The sample applied magnetic field was set to zero. The double-tilt TEM holder equipped with He cooling system (Gatan Inc.) was adopted for the specimen cooling and the observation was performed at a display temperature of 5.5 K.

Figures 6 **a** and **b** show the results of the DPC STEM observation. Grain-like contrast is observed in both **a**, the transverse field image and **b**, the longitudinal field image. These are also observed at room temperature, and the low spatial frequency contrast is superimposed on the low magnification HAADF image shown in Fig. 4**a**. These suggest that this contrast could be caused by surface damage during TEM sample preparation.

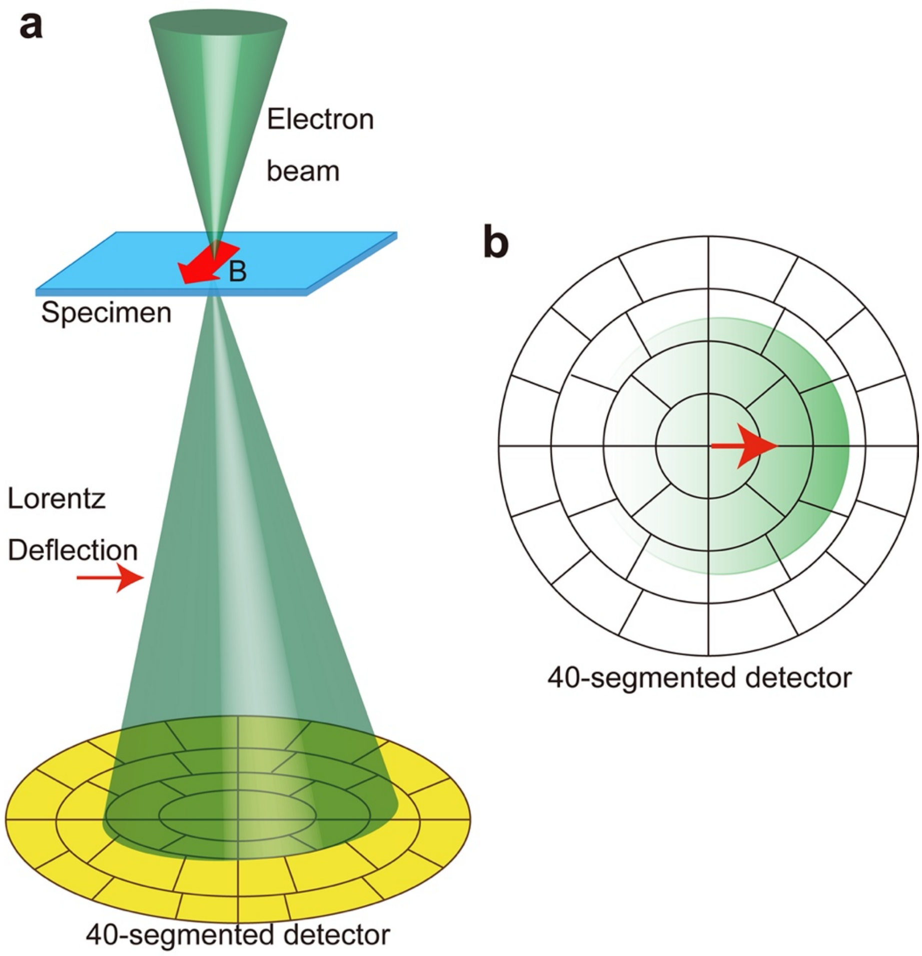

Fig. 5: Schematics of **a**, DPC STEM and **b**, transmitted electron disk deflected by the sample magnetic field and a segmented detector.

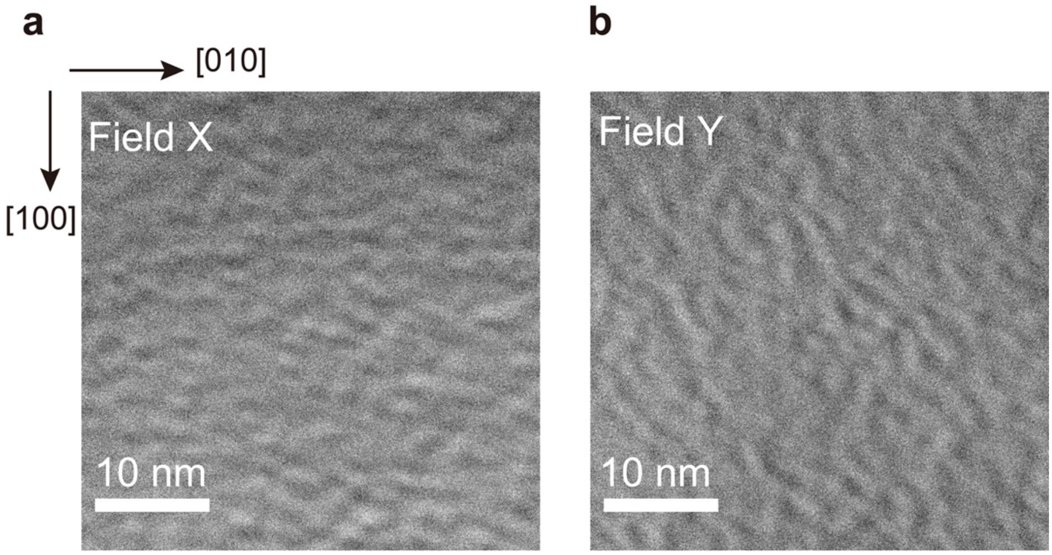

Fig. 6: DPC images of the $GdRu_2Ge_2$ sample. Images of the magnetic field in the [010] and [100] directions are shown in **a** and **b**, respectively. The rightward and downward magnetic fields in **a** and **b** are shown as bright contrasts, respectively.

Conclusions and Future prospects

In this study, we synthesized $GdRu_2Ge_2$ and performed sample evaluation by X-ray diffraction. After that, the structural and magnetic field observations in real-space were performed by STEM. As a result, it was confirmed that the target sample had the intended crystal structure. On the other hand, magnetic structures were not observed in this experiment. The candidate reason for these results could be the amorphous damage during the process of TEM sample preparation. As future prospects, we are considering optimizing the method of the TEM sample preparation and conducting high-resolution observation of the magnetic structure with/without applying magnetic field. If these experiments can be performed, it is expected that the complex magnetic phases in $GdRu_2Ge_2$ are visualized in real-space.

Acknowledgement

We express our sincerest gratitude to the author's advisors, Prof. Shibata and Prof. Shinichiro Seki from the University of Tokyo, for enlightening guidance and fruitful advice. We appreciate Dr. Takehito Seki, Dr. Takagi and Mr. Iwata for supporting us. We would also like to appreciate the MERIT advisor, Prof. Tanaka for giving the permission to proceed with the research. In the end, we would like to express our sincere gratitude to MERIT program for giving us a great opportunity for this joint research.

Reference

1. Mühlbauer, S. *et al.* Skyrmion Lattice in a Chiral Magnet. *Science* **323**, 915–919 (2009).
2. Yu, X. Z. *et al.* Real-space observation of a two-dimensional skyrmion crystal. *Nature* **465**, 901–904 (2010).
3. Jonietz, F. *et al.* Spin Transfer Torques in MnSi at Ultralow Current Densities. *Science* **330**, 1648–1651 (2010).
4. Fert, A., Reyren, N. & Cros, V. Magnetic skyrmions: advances in physics and potential applications. *Nat. Rev. Mater.* **2**, 17031 (2017).
5. Seki, S., Yu, X. Z., Ishiwata, S. & Tokura, Y. Observation of Skyrmions in a Multiferroic Material. *Science* **336**, 198–201 (2012).
6. Nagaosa, N. & Tokura, Y. Topological properties and dynamics of magnetic skyrmions. *Nat. Nanotechnol.* **8**, 899–911 (2013).
7. Tokunaga, Y. *et al.* A new class of chiral materials hosting magnetic skyrmions beyond room temperature. *Nat. Commun.* **6**, 7638 (2015).
8. Kézsmárki, I. *et al.* Néel-type skyrmion lattice with confined orientation in the polar magnetic semiconductor GaV4S8. *Nat. Mater.* **14**, 1116–1122 (2015).
9. Nayak, A. K. *et al.* Magnetic antiskyrmions above room temperature in tetragonal Heusler materials. *Nature* **548**, 561–566 (2017).
10. Hayami, S., Ozawa, R. & Motome, Y. Effective bilinear-biquadratic model for noncoplanar ordering in itinerant magnets. *Phys. Rev. B* **95**, 224424 (2017).
11. Hayami, S. & Motome, Y. Topological spin crystals by itinerant frustration. *J. Phys. Condens. Matter* **33**, 443001 (2021).
12. Hayami, S. & Motome, Y. Square skyrmion crystal in centrosymmetric itinerant magnets. *Phys. Rev. B* **103**, 024439 (2021).
13. Kurumaji, T. *et al.* Skyrmion lattice with a giant topological Hall effect in a frustrated triangular-lattice magnet. *Science* **365**, 914–918 (2019).
14. Hirschberger, M. *et al.* Skyrmion phase and competing magnetic orders on a breathing kagomé lattice. *Nat. Commun.* **10**, 5831 (2019).
15. Khanh, N. D. *et al.* Nanometric square skyrmion lattice in a centrosymmetric tetragonal magnet. *Nat. Nanotechnol.* **15**, 444–449 (2020).
16. Yasui, Y. *et al.* Imaging the coupling between itinerant electrons and localised moments in the centrosymmetric skyrmion magnet GdRu2Si2. *Nat. Commun.* **11**, 5925 (2020).
17. Yoshimochi, H. *et al.* in preparation.
18. Shibata, N. *et al.* Direct Visualization of Local Electromagnetic Field Structures by Scanning Transmission Electron Microscopy. *Acc. Chem. Res.* **50**, 1502–1512 (2017).
19. Shibata, N. *et al.* Imaging of built-in electric field at a p-n junction by scanning

transmission electron microscopy. *Sci. Rep.* **5**, 10040–10040 (2015).
20. Toyama, S. *et al.* Quantitative electric field mapping of a p–n junction by DPC STEM. *Ultramicroscopy* **216**, 113033–113033 (2020).
21. Shibata, N. *et al.* Differential phase-contrast microscopy at atomic resolution. *Nat. Phys.* **8**, 611–615 (2012).
22. Ishikawa, R. *et al.* Direct electric field imaging of graphene defects. *Nat. Commun.* **9**, 3878–3878 (2018).
23. Kohno, Y., Seki, T., Findlay, S. D., Ikuhara, Y. & Shibata, N. Real-space visualization of intrinsic magnetic fields of an antiferromagnet. *Nature* **602**, 234–239 (2022).
24. Matsumoto, T., So, Y. G., Kohno, Y., Ikuhara, Y. & Shibata, N. Stable Magnetic Skyrmion States at Room Temperature Confined to Corrals of Artificial Surface Pits Fabricated by a Focused Electron Beam. *Nano Lett.* **18**, 754–762 (2018).
25. Shibata, N. *et al.* Atomic resolution electron microscopy in a magnetic field free environment. *Nat. Commun.* **10**, 2308–2308 (2019).
26. Garnier, A., Gignoux, D., Schmitt, D. & Shigeoka, T. Giant magnetic anisotropy in tetragonal GdRu2Ge2 and GdRu2Si2. *Phys. B Condens. Matter* **222**, 80–86 (1996).
27. Pennycook, S. J. & Jesson, D. E. High-resolution incoherent imaging of crystals. *Phys. Rev. Lett.* **64**, 938–941 (1990).
28. Pennycook, S. J. & Jesson, D. E. High-resolution Z-contrast imaging of crystals. *Ultramicroscopy* **37**, 14–38 (1991).
29. Lippmann, B. A. Ehrenfest's Theorem and Scattering Theory. *Phys. Rev. Lett.* **15**, 11–14 (1965).
30. Waddell, E. M. Linear imaging of strong phase objects using asymmetrical detectors in STEM. *Opt. Stuttg.* **54**, 83–83 (1979).
31. Close, R., Chen, Z., Shibata, N. & Findlay, S. D. Towards quantitative, atomic-resolution reconstruction of the electrostatic potential via differential phase contrast using electrons. *Ultramicroscopy* **159**, 124–137 (2015).